Journal Name

ARTICLE

Addressing the Characterisation Challenge to Understand Catalysis in MOFs: The Case of Nanoscale Cu Supported in NU-1000

Received 00th January 20xx,
Accepted 00th January 20xx

DOI: 10.1039/x0xx00000x

www.rsc.org/

Ana E. Platero-Prats,[a] Zhanyong Li,[b] Leighanne C. Gallington,[a] Aaron W. Peters,[b] Joseph T. Hupp,[b] Omar K. Farha[b,c] and Karena W. Chapman[a]

We explore the dynamic structure and reactivity of Cu species supported on NU-1000. By combining pair distribution function (PDF) analysis and difference envelope density (DED) analysis of *in-situ* synchrotron-based X-ray scattering data, we simultaneously probe the local structure of supported Cu-species, their distribution within NU-1000 and distortions of the NU-1000 lattice under conditions relevant to catalysis and catalyst activation. These analyses show that atomic layer deposition (ALD) of Cu in NU-1000 (Cu-AIM) leads to the formation of Cu-oxo clusters within the small pores that connect the triangular and hexagonal channels. Exposure of Cu-AIM to reducing atmosphere at 200 °C produces metallic Cu^0 of two distinct particle sizes: ~4 nm nanoparticles and small sub-nanometer clusters. The size of these nanoparticles appear to be constrained by NU-1000 pore dimensions, with evidence of the sub-nanometer clusters being bound within the triangular channels flanked by pyrene rings. This supported Cu^0-NU-1000 system is catalytically active for gas-phase ethylene hydrogenation. Exposure of the catalyst to oxidative atmosphere re-oxidises the Cu species to a Cu_2O cuprite phase. The dynamic restructuring of the system in different chemical environments underscores the importance of probing these systems in-situ.

Introduction

Crystalline nanoporous solids with high internal surfaces areas are widely used as catalysts and catalyst supports. While porous zeolites have been widely explored for catalytic applications,[1] metal-organic frameworks (MOFs), an emerging class of nanoporous crystalline solid, have demonstrated recent promise in this area.[2, 3] The richly versatile MOF structures and surface chemistries can be effective in catalysing chemical reactions or can be adapted to different catalytic reactions through post-synthetic modification,[4] including through solvent-phase impregnation and/or vapour-phase deposition such as atomic layer deposition (ALD).[5,6, 7,8-12] The large internal surface of MOFs provides a large active surface are for catalytic reactions with the further potential for the pore geometries and architectures to confine the geometry of reagents/products and the distribution of supported catalytic species. Understanding the structure and distribution of catalytic sites within MOF catalysts and catalyst supports is critical to developing a mechanistic understanding of their catalytic activity and, hence, fully optimising their catalytic performance.

While MOFs adopt ordered crystalline structures and, indeed, often form as single-crystals for which the precise atomic structure can be routinely determined using X-ray crystallography, the dynamic nature of their structure and supported catalytic species under conditions relevant to catalytic functionalisation and reactions often complicates structure characterisation to understand the catalytic function is a substantial challenge. For applications, MOF are typically prepared as small crystallites (i.e., powders) that are too small for structural analysis through single crystal diffraction. Under reaction conditions, the crystallinity and ordering of the MOF often reduces which broadens the diffraction peaks and limits the structural details that can be resolved. With catalysis being a local phenomenon, how local structures deviate from the average, ordered structure can play an important role in the reactivity. While understanding both the local and average structure within the MOF is a characterisation challenge, addressing this challenge is central to developing an understanding their structure-activity relationship. In this endeavour, incisive experiments that use advanced characterization tools to probe the local structure and dynamic states of MOFs *in-situ*, during reactions, are of central importance.[13,14, 15]

In the development of MOF-based catalysts, robust Zr-based MOFs connected *via* strong Zr^{IV}-O bonds[16, 17] that tolerate catalytic reaction conditions and chemical functionalisation, are promising systems[6] that avoid instabilities that can limited other MOFs. NU-1000 is a large pore Zr-based MOF that is a versatile platform for developing MOF-based catalysts.[9] NU-

[a] *X-ray Science Division, Advanced Photon Source, Argonne National Laboratory, Argonne, Illinois 60439-4858, United States.*
[b] *Department of Chemistry, Northwestern University, Evanston, Illinois 60208-3113, United States.*
[c] *Department of Chemistry, Faculty of Science, King Abdulaziz University, Jeddah, Saudi Arabia*

1000 is formed by robust $Zr_6O_4(\mu\text{-}OH)_4$-based nodes[18] connected through pyrene-based tetracarboxylate ligands (Figure 1). Hexagonal and triangular channels of diameters ~32 Å and ~10 Å, respectively, aligned parallel to the c-axis, are connected *via* small pores of ~8×10×10 Å. These small pores are bounded in the *c*-direction by the Zr_6-based nodes. While NU-1000 is active as an acid catalyst,[5] it has broader potential as a catalytic-support—a wide variety of metal species can be deposited at ordered sites throughout the framework. ALD in NU-1000, involving reaction of organometallic precursors with the hydroxyl sites on the Zr_6-based nodes, allows a wide variety of metal-oxo clusters to be deposited within the small pores of NU-1000.[9, 15] These include Al-AIM,[9] Zn-AIM,[9, 15] (AIM, ALD in MOFs), In-AIM,[19] Ni-AIM,[10] and Co-AIM.[8]

Here we combined in-situ pair distribution function (PDF) and diffraction analyses of high-energy synchrotron X-ray scattering data to explore the structural changes that occur in a Cu-functionalised NU-1000, prepared through ALD (Cu-AIM), under conditions relevant to catalysis and catalyst activation. The PDF provides local structural information, independent of long range ordering, as a weighted histogram of all atom-atom correlations within the system. Complementary difference envelope density (DED) analysis of the broadened X-ray powder diffraction data provides a low-resolution map of the distribution of the species within the NU-1000 pores. By combining insights from these local and average structure probes, we demonstrate a reversible formation of metallic copper clusters and nanoparticles within Cu-AIM under conditions relevant to their use in ethylene hydrogenation catalysis.

Experimental

Synthesis procedures. The synthesis of Cu-AIM[20] follows similar procedures as previous metal-AIM syntheses.[1] Atomic layer deposition was undertaken using a Savannah 100 (Cambridge Nanotech, Inc). The Cu precursor, bis(dimethylamino-2-propoxy)copper(II) ($Cu(dmap)_2$, reactant A), was used as received from Strem Chemicals. Microcrystalline NU-1000 (as hexagonal rods, 0.6x0.6x3-5 µm) was prepared as described previously.[9] Room temperature deionized H_2O was used as the co-reactant (reactant B). In a typical experiment, a custom-made stainless steel sample holder containing microcrystalline NU-1000 (60.0 mg, 0.028 mmol) was placed in the ALD chamber, which was held at 110 °C for 30 min to remove physisorbed water before dosing with the Cu precursor. A cylinder containing $Cu(dmap)_2$ was held at 100 °C, and each of its pulses followed the time sequence of t_1–t_2–t_3, where t_1 is the precursor pulse time, t_2 is the substrate exposure time, and t_3 is the N2 purge time (t_1 = 1 s, t_2 = t_3 = 240 s). To ensure complete metalation at all Zr_6 sites, the $Cu(dmap)_2$ pulsing cycle was run 80 times before exposing the MOF to H_2O pulses, adopting the same pulse sequence as for Cu (t_1 = 0.015 s, t_2 = t_3 = 120 s).

The Cu concentration in Cu-AIM was determined by inductively coupled plasma–atomic emission spectroscopy (ICP–AES).

X-ray Photoelectron Spectroscopy (XPS).
X-ray photoelectron spectroscopy (XPS) measurements were carried out at the KECK-II/NUANCE facility at NU on a Thermo Scientific ESCALAB 250 Xi (Al K_α radiation, hv = S5 1486.6 eV) equipped with an electron flood gun. XPS data were analysed using Thermo Scientific Avantage Data System software and all spectra were referenced to the C 1s peak (284.8 eV).

Gas phase catalysis.

The gases used for gas-phase hydrogenation catalysis were 3% ethylene balanced with Ar, 5% H_2 balanced with Ar, and ultra-high purity Ar.
The catalyst (~20 mg Cu-AIM, ~4.5:6 Cu/Zr, 13 wt% Cu, diluted with ~200 mg of SiO_2) was packed on quartz wool in a stainless reactor. The reaction temperature was controlled with a K-type thermocouple at the top of the catalyst bed. For the catalyst pre-treatment procedure, the temperature was ramped at 10 °C/min to a final temperature of 200 °C under a flow of 200 mL/min 5% H_2/Ar (1.5 bar pressure) for 2 h. It was then cooled to the desired temperature (150 °C) under a flow of 200 mL/min Ar within 1 h. For the catalysis, the ratio of flow rates between the two reacting gases and Ar were kept constant for all the experiments (C_2H_4: H_2: Ar = 1:2:3).

Synchrotron X-ray scattering (XRD and PDF). Quasi-simultaneous X-ray diffraction data and total scattering data suitable for PDF analysis were collected at 11-ID-B beamline at the Advanced Photon Source at Argonne National Laboratory using 58.6 keV (0.2114 Å) X-rays. Data were collected using an amorphous silicon-based area detector. For powder diffraction analysis, data were collected at long sample-to-detector distance (~95 cm) to optimize the 2-theta angular resolution. For PDF analysis, data were collected at short sample-to-detector distance (~20 cm) to maximize the *Q*-range. Geometric corrections and reduction to one-dimensional data were performed using FIT2D.[21] For controlled atmosphere and variable temperature measurements, powder samples were loaded into borosilicate capillaries, assembled into a flow cell.[22, 23] To assess structural changes under reducing atmosphere, samples were heated from 50 to 350 °C at 5 °C min^{-1} under a flow of diluted H_2 (3.5% in He). To assess structural changes under reaction conditions, samples were heated from 50 to 200 °C at 5 °C min^{-1} under diluted H_2 (3.5% in He), held at 200 °C for 2 h and cooled to 50 °C under a mixture flow of ethylene in diluted H_2 (1:2 ratio).

Lattice parameters and peak intensities were extracted from diffraction patterns via Le Bail whole pattern fitting[24, 25] using Jana2006,[26] based on the reported structural model for NU-1000 (P6/mmm, a ~ 40 Å, c ~ 17 Å).[9] Lattice and pseudo-Voigt profile parameters were refined over a 0.5-10° 2θ range. Structure envelopes were generated using the intensities of low index reflections.[27, 28] Difference envelope densities (DEDs) were then obtained via subtraction of the envelope for pristine NU-1000 from the envelope for Cu-AIM under different conditions.[29]

PDFs were obtained from the data using PDFgetX2[30] to Q_{max}=22 $Å^{-1}$. Differential PDFs for Cu-AIM were calculated by subtracting

the PDF of system before ALD or before nanoparticle formation. Structural models were refined against the PDF data with PDFgui[31] to estimate the nanoparticle size.

Results

Synthesis and Structure of Cu-AIM.

Compositional analysis through ICP-AES indicates that an average 4.5 Cu atoms are deposited per Zr_6-based node in Cu-AIM.

The location of Cu-oxo species deposited within the crystalline NU-1000 lattice through ALD was evaluated through DED analysis of powder diffraction data. The DED analysis shows that the Cu-oxo species are deposited as clusters localised in the small pores of NU-1000 (Figure 1), between pairs of Zr_6-based nodes. A similar localised deposition of metal-oxo clusters *via* AIM as has been previously observed in Zn-AIM.[15]

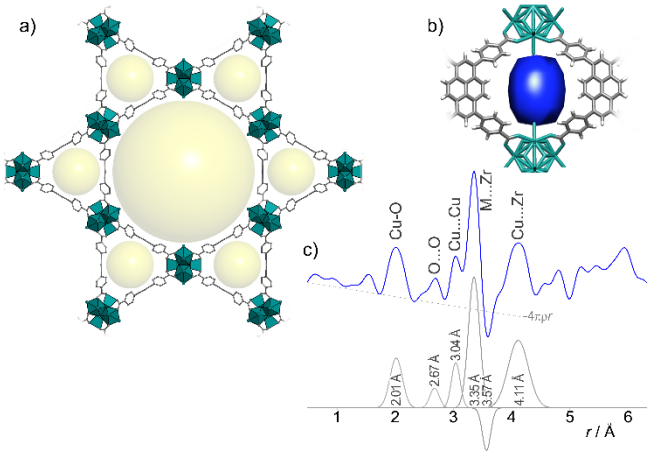

Figure 1. a) A representation of the NU-1000 framework, view parallel to the *c* axis. The 3- and 1-nm-diameter hexagonal and triangular channels, respectively, are shown in yellow. b) The DED map, viewed perpendicular to the *c* axis, showing the location of the Cu-oxo clusters deposited in the NU-1000 small pores between the Zr_6-based nodes. c) The differential PDF corresponding to new and modified atom-atom distances in Cu-AIM.

The local atomic structure of the Cu-oxo clusters was probed using differential PDF analysis, which selectively recovers the new and modified atom-atom distances within Cu-AIM following ALD. The differential PDF showed a peak at 2.01 Å that corresponds to the average Cu–O bonds (Figure 1); the broad nature of the peak suggests a distribution of Cu-O bond lengths and geometries. Peaks at 2.67 Å and 3.04 Å likely reflect new O…O and Cu…Cu for corner-shared CuO_6 octahedra, respectively. The differential PDF included a feature below the −4πρr baseline at 3.57 Å, the Zr…Zr distance in pristine NU-1000. This has previously been recognised as an effect of a symmetry-lowering distortion of the Zr_6-based nodes in Zr-based MOFs upon dehydration at elevated temperature. A large peak at 3.35 Å likely contains contribution from Zr…Zr correlations in the newly distorted nodes following ALD, as well as Cu…Zr correlations for Cu-oxo species bound to the node.

Oxidation state of Cu in Cu-AIM. X-ray photoelectron spectroscopy (XPS) suggests that the Cu within Cu-AIM exists predominantly in the divalent state**.** Satellite features characteristic of Cu^{2+} are observed at 940 and 960 eV (Figure 2). Upon heating in reducing atmosphere (200 °C, 3.5% H_2 in Ar), these satellites disappear with the feature associated with Cu $2p_{3/2}$ shifting to lower binding energy, as is consistent with the reduction of Cu^{2+} to Cu^{1+} or Cu^0. Re-oxidation of the Cu is evident upon subsequent exposure to air: features associated with Cu^0 re-emerging after 5 min air exposure (Figure 2).

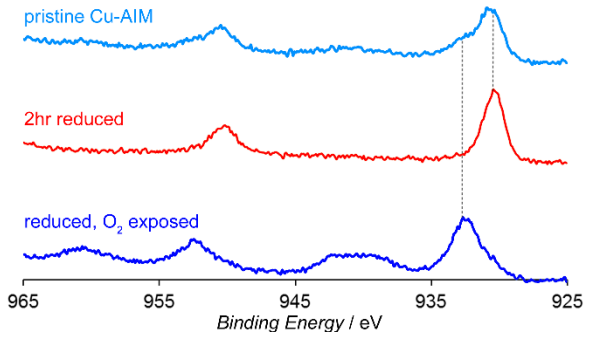

Figure 2. XPS spectra of Cu-AIM as-prepared, reduced, and reduced after air exposure.

PDF analysis of nanoparticle formation during reduction

To explore the structural changes that occur in Cu-AIM under conditions relevant to catalysis and catalyst activation, in-situ PDF and diffraction data were collected under controlled temperature and gas atmosphere. Two separate variable temperature/atmosphere profiles were evaluated. One Cu-AIM sample was heated to 350 °C at 5 °$Cmin^{-1}$ under 3.5% H_2 in He then cooled to room temperature. A second Cu-AIM was heated at 200 °C at 5 °$Cmin^{-1}$ under 3.5% H_2 in He, held at 200 °C under 3.5% H_2 in He for 2 h, cooled to 50 °C under 3.5% H_2 in He at 5 °$Cmin^{-1}$, exposed to He, then reactive gases at 50 and 200°C, then exposed to air.

In the PDF for Cu-AIM (Figure 3), well-defined peaks are only observed at short atom-atom distances (below ~8 Å), as is consistent with the reduced crystallinity following ALD. Broad diffuse features in the PDF at longer distances reflect the modulating electron density of the porous framework structure.

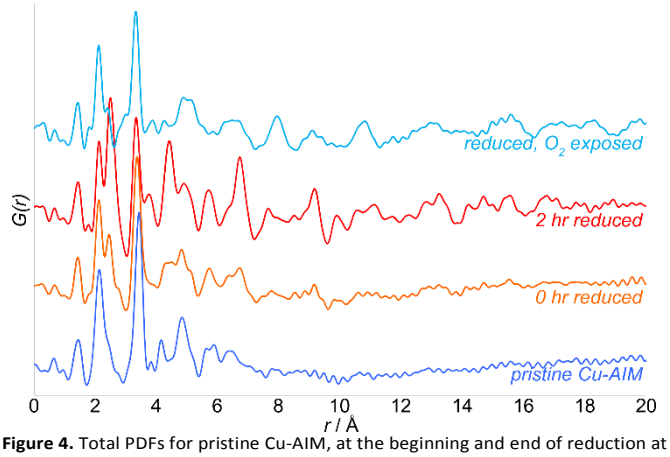

Figure 4. Total PDFs for pristine Cu-AIM, at the beginning and end of reduction at 200 °C and following re-oxidation upon exposure to air.

Upon heating to 350°C, the PDF data show few changes below ~190 °C, beyond a slight shift of the peak at ~3.5 Å that reflects

an increasing distortion of the Zr-based nodes. At 210 °C new peaks appear at ~2.5 Å and at longer distances corresponding to Cu…Cu distances in metallic Cu^0 nanoparticles with a face-centred cubic (fcc) structure. For data collected at 190 °C, immediately preceding the formation Cu^0 nanoparticles, weak features consistent with a small amount of a nanoscale Cu^I_2O phase was evident in the PDF.

For the sample held at 200°C under reducing atmosphere (3.5% H_2 in He), the gradual growth of features associated with Cu^0 nanoparticles is observed (Figure 3). For structural refinements, differential PDFs were calculated by subtracting the PDF obtained immediately before Cu^0 nanoparticles were observed, from PDFs where nanoparticles are first observed, at the end of the reduction at 200 °C and following exposure to air. These differentials highlight the contribution from the new supported species formed during reduction, associated changes to the NU-1000 structure and species consumed by the reduction. A large negative feature in the differential PDFs at ~3.57 Å is again indicative of increased distortion of the Zr_6-based nodes,[32] which appears to occur in concert with the Cu reduction.

Refinements of a structural model for fcc Cu^0 nanoparticles against the differential PDF data provided an estimate of the average nanoparticle size using a spherical particle model (Figure 4a). Initial refinements used PDF data in the range ~8-30 Å, beyond the well-defined atom-atom contributions from the NU-1000 framework. An average Cu^0 particle dimension of ~4 nm was found at the beginning and end of reduction. These nanoparticles were retained upon cooling to 50 °C. Calculation of the PDF for the Cu^0 nanoparticle model to low *r* revealed additional features in the residual (Figure 4a, inset) suggestive of a second population of Cu^0 clusters of smaller sub-nanometer size. The longest well-defined peak, in these sub-nanometer clusters, was observed at 6.7 Å. Including these clusters in the model being refined against the PDF data suggest that approximately half the reduced Cu^0 exists in these clusters. During the isothermal reduction, the quantity of Cu^0 increases by 50% relative to the initial amount observed in the first data set at 200 °C. The distribution of Cu^0 in the nanoparticles and sub-nanometer clusters does not change significantly.

With subsequent exposure to helium then reaction conditions for ethylene hydrogenation (ethylene+H_2) or air, the Cu^0 is re-oxidised to form Cu_2O nanoparticles of ~4 nm diameter. The oxidation of the sample in helium likely reflects trace O_2 impurities in the gas and the small sample volume used here.

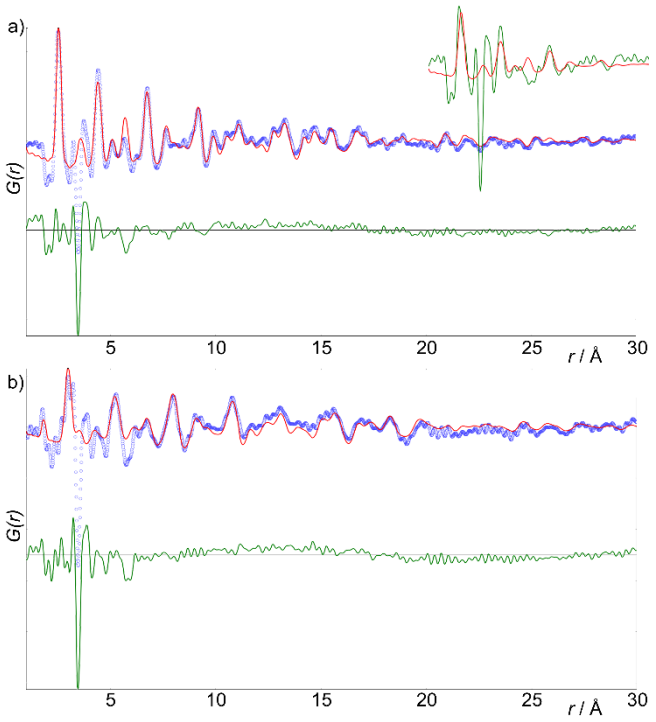

Figure 3. Fits of models for a) fcc Cu^0 (sub-nanometer clusters and 4nm nanoparticles) and b) Cu_2O nanoparticles to differential PDFs obtained by subtracting the total PDF before nanoparticles form from that at the end of reduction and following air exposure, respectively. Features in the residual reflect unmodelled species and changes to the framework. (a, inset) A residual (green) to a fit where only the 4 nm nanoparticles were modelled and the PDF for the Cu^0 cluster model (red).

Distribution of supported Cu species on NU-1000.

The powder diffraction data, collected in parallel with the PDF data, show a discontinuity in the lattice parameters upon nanoparticle formation without loss of crystallinity (Figure 5). The *c*-lattice parameter expands, while the *a*-lattice parameter contracts, reversing the change in lattice dimension that occurs during ALD.[15] While the largest change in lattice is associated with the initial nanoparticle formation, these changes continue progressively during the isothermal treatment.

Journal Name

ARTICLE

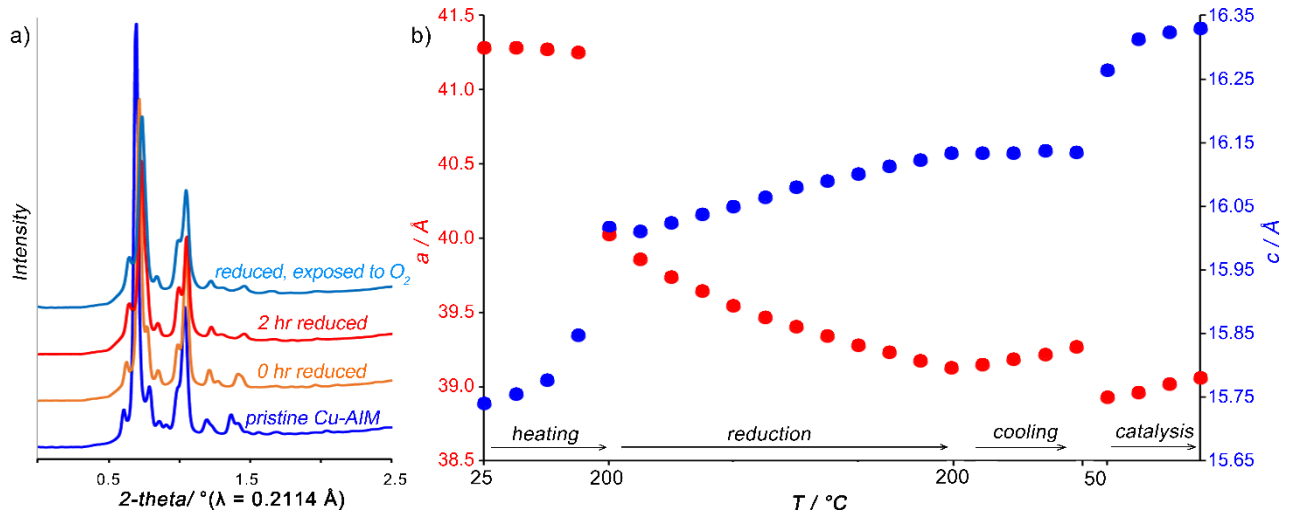

Figure 5. a) XRD data for Cu-AIM in the pristine state, at the beginning and end of reduction at 200 °C and following re-oxidation. b) Refined lattice parameters for Cu-AIM during heating, reduction for 2 hr at 200 °C, cooling under H_2 and under catalytic reaction conditions.

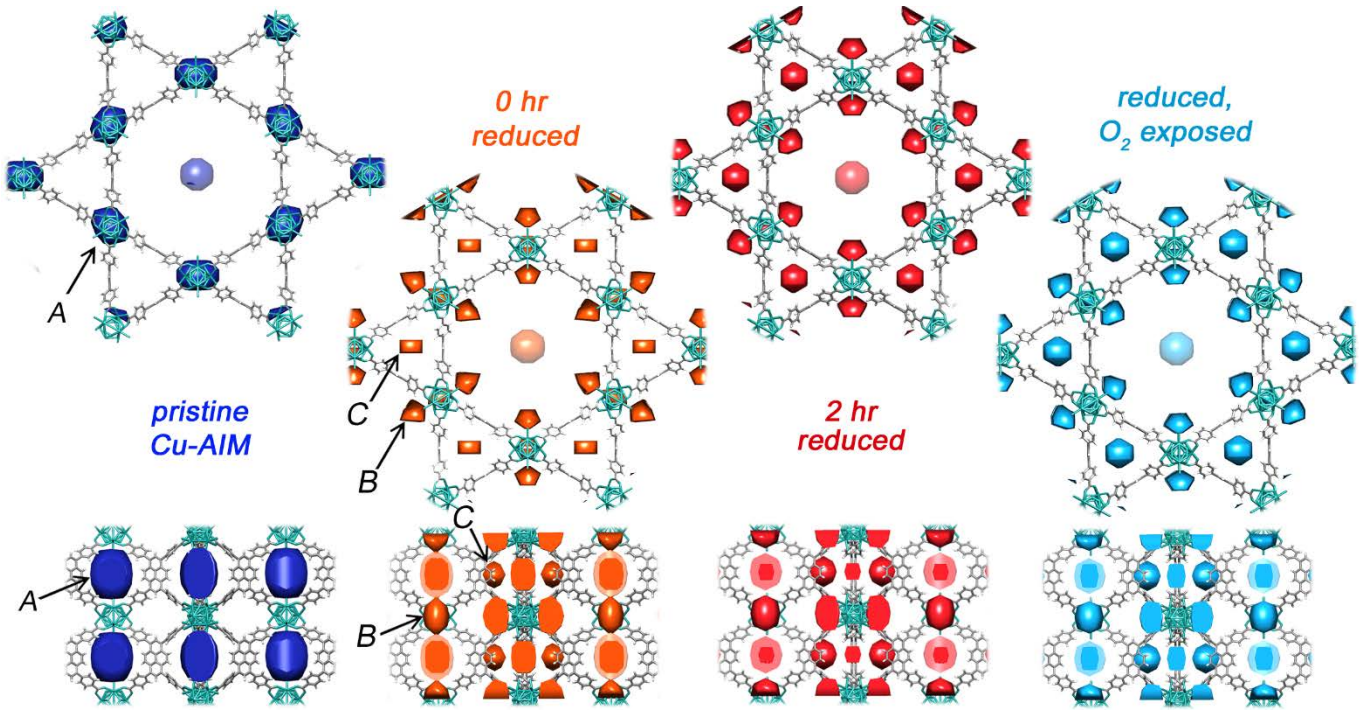

Figure 6. DED maps viewed parallel (top) and perpendicular (bottom) to the c-axis for Cu-AIM in the pristine state, at the beginning and end of reduction at 200 °C and following re-oxidation.

DED analyses were performed to evaluate the distribution of the supported Cu species within the NU-1000 pores (Figure 6). With heating under reducing atmosphere, no changes are observed in the DED prior to the observation of Cu^0 nanoparticles in the PDFs. The deposited Cu species remain predominately as clusters in the small cavity bridging the Zr_6-based nodes along the c-axis (site A). An artefact centred within the hexagonal channel is observed in all DEDs; it does not change throughout the reduction and re-oxidation.

A substantial redistribution of the Cu species occurs in concert with the appearance of Cu^0 nanoparticles. Qualitatively similar changes are evident in the samples heated to 350 °C and during reduction at 200 °C; a more gradual evolution is evident during the latter, isothermal treatment. Electron density in the cavity between Zr_6-based nodes progressively disappears (site A). New electron density is observed adjacent to the Zr_6-node faces in the hexagonal channel (site B) and in the triangular channel between the pyrene groups (site C). During the isothermal reduction, the electron density centered at site C increases with indications of increased electron density broadly distributed throughout the hexagonal channel (Figure 7). The electron density does not change significantly upon re-oxidation of the sample, although the DED between the reduced and oxidized states, suggests a small loss in intensity from site C.

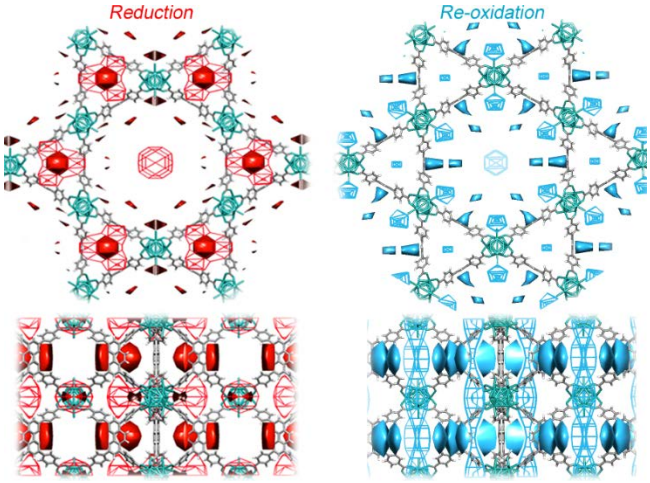

Figure 7. DED maps viewed parallel (top) and perpendicular (bottom) to the c-axis, corresponding to the changes in electron density for Cu-AIM during isothermal reduction at 200 °C and subsequent re-oxidation. Regions of increased electron density are shown as a solid surface and regions of reduced electron densities are shown as a mesh.

Catalysis.

With Cu^0 species known to be active hydrogenation catalysts,[33,34] gas-phase ethylene hydrogenation catalysis was evaluated in Cu-AIM. The as-prepared Cu-AIM showed no catalytic activity under the testing conditions. Upon reduction of Cu-AIM under H_2 flow at 200 °C for 2 h, the material becomes active for ethylene hydrogenation catalysis. By varying the space velocity of ethylene, the turnover frequency (TOF) for the process catalysed by Cu-AIM was established to be 0.40±0.04 h^{-1} at 150 °C (Figure 8).

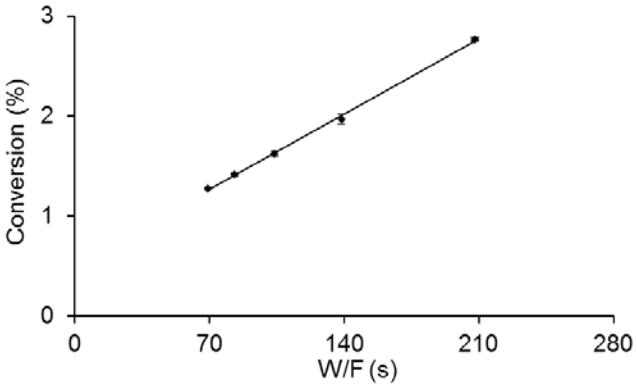

Figure 8. Determination of the TOF for the ethylene hydrogenation process catalysed by the in-situ reduced Cu-AIM sample.

Discussion

The reversible Cu reduction and nanoparticle formation observed in Cu-AIM, demonstrates the dynamic nature of the supported Cu species in NU-1000. Once the threshold temperature for reduction has been attained (~200 °C), reduction proceeds rapidly. The reduction temperatures observed here are similar to temperatures at which reduction has previously been observed in supported CuO/ZrO_2 systems.[35,36] The observation of Cu_2O as an intermediate in the reduction is typical of reactions under limited flow of reducing gas.[37] This reduction sequence has been previously observed for bulk CuO under kinetically-controlled regimes and could be explained here by a limited H_2 diffusion through the pores.[37] In the present system, there is clearly two different time-scales relevant to the reduction: there is an initial rapid reduction once a threshold temperature has been achieved and there is a slower reduction that occurs progressively during isothermal treatment. Additional studies with finer time resolution and/or at lower temperature may be valuable in understanding the detailed mechanism for Cu^0 reduction and nanoparticle at the onset of reduction. Complementary studies of Cu-AIM, centred largely on X-ray Absorption Spectroscopy measurements, have been pursued by colleagues and will be reported elsewhere.[38]

The ALD-deposited Cu-oxo clusters in NU-1000 serve as Cu^0 precursors: reduction of the clusters produces size-limited Cu^0 species without destroying the MOF framework. Of the Cu^0 formed at 200 °C two-thirds is observed immediately upon reaching 200 °C, with a further one-third formed during the isothermal treatment. This is also reflected in the relative changes in the lattice parameters.

While there is an increase in the Cu^0 population during reduction, the distribution of Cu^0 species, between sub-nanometer clusters and 4 nm nanoparticles does not change and there are no new sites in the DEDs. Very small, sub-nanometer Cu^0 clusters would not be expected to persist, over the long times seen here, unless they were appropriately stabilized or confined. We propose that the sub-nanometer clusters (an estimated 12-20 Cu^0 atoms) are confined by the NU-

1000 pores, and occupy the pyrene pocket in the triangular channels (site C in the DED). Such metallic clusters may be expected to have favourable interactions with the aromatic pyrene rings surrounding this site with metal surface to aromatic ring distances of 2.5-3 Å.[39] These would form following reduction and aggregation of the three Cu-oxo clusters surrounding the pyrene pocket.

Both the Cu^0 clusters and nanoparticles can contribute to the observed ethylene hydrogenation catalysis. With a higher surface area to volume ratio, the sub-nanometer clusters may be expected to be more active on a per Cu atom basis.

The rapid appearance of the Cu^0 nanoparticles demonstrates the high mobility of the reduced Cu-species on the MOF surface. Aggregation as large nanoparticles requires that Cu species diffuse over long distances, across both inorganic and aromatic organic surfaces. Given the high mobility of the Cu^0 species and rapid formation of the Cu^0 nanoparticles, it is surprising that the nanoparticles do not continue to grow further and aggregate as larger particles.

While the average nanoparticle dimension observed here is larger than the ~3 nm diameter of the hexagonal channels within NU-1000, we cannot conclude that the Cu^0 has migrated to the outer surface of the MOF. If a significant fraction of the Cu^0 nanoparticles had diffused to the outer surface of the MOF, there would be little impediment to further aggregation and larger Cu nanoparticles would be expected.[40] We propose that the apparent difference in the nanoparticle and pore dimensions may be a combined consequence of approximating the size of an undulating channel based on the dimension at the narrowest point and estimating the nanoparticle dimensions using a spherical particle model. While the narrowest aperture defined by the hexagonal channels is 3 nm diameter, at the widest parts of the channel nanoparticles could extend into the small pores that link the hexagonal and triangular channels such that nanoparticle that span >3 nm could be accommodated. Further, while the average dimension of the Cu^0 nanoparticles is 4 nm, if the nanoparticles were elongated (i.e. as prolate spheroids of ≥4 nm along the longest dimension) then they may be still be accommodated within narrower channels. In this case, continued growth of the nanoparticles could be limited by the amount of Cu within an accessible crystal volume and/or confinement by the NU-1000 framework. Favourable interactions of the NU-1000 surface and selected facets of the Cu particles, for example, with stronger physisorptive-like interactions of aromatics (in this case the pyrene component of the tetracarboxylate ligand) with the Cu(110) rather than Cu(111)[39]) may further facilitate the Cu particle confinement. However, the possibility remains that some large nanoparticles have vacated the channels and are located on the outer surface of the NU-1000 particles (to which the DED analysis is blind), and that a different, unanticipated mechanism is responsible for nanoparticle size confinement.

It is not clear how the picture of nanoparticle confinement correlates with the features in the DED found in the hexagonal channels (site B), where the new electron density is small and localized on the Zr_6-based nodes. Disordered distribution of large nanoparticles within the pores may give rise to the observed pattern. Considering distribution of Cu within pristine Cu-AIM (4.5 Cu/node) and the number of Cu^0 atoms within a 4 nm particle (*ca.* 2900), if all the Cu on nodes surrounding a single hexagonal channel were to form 4 nm nanoparticles within that channel, the Cu would have aggregated over ~110 unit cells or 180 nm. The average occupancy of nanoparticles per unit cell would be less than 1%, so it is unsurprising that large features corresponding to these nanoparticles are not clearly observed in the DED. While nanoparticle sintering as a result of metal diffusion and re-oxidation is known in zeolites and other related materials,[41] the observation of metal transport across the heterogeneous surface of NU-1000 is somewhat unexpected, particularly in a system without high ionic or electronic conductivity.

That the NU-1000 framework is not disrupted by the Cu reduction and nanoparticle formation is a testament to the robust nature of this system. Flexible MOFs[40, 42] have demonstrated similar tolerance to nanoparticle formation. The NU-1000 framework tolerates the rapid rearrangement of copper sites followed by the formation of nanoparticles and indeed confines the nanoparticle. By contrast, in earlier studies of metal nanoparticle formation within MOFs, nanoparticles that grow to exceed the pore dimensions by several times is more typically observed. [11, 43-45]

Despite the robust nature of the framework, distortions of the Zr_6-based nodes of are evident both following ALD to deposit Cu-oxo species in the small pore and following reduction which eliminates the Cu-oxo species from these pores. The degree of distortion evident following ALD is substantially less than that observed following thermal dehydration/dehydroxylation of the nodes, although the ALD reaction is also associated with dehydration/dehydroxylation.[32] We propose that coordination of the Cu-oxo clusters at the Zr_6-based node during may inhibit full distortion of the node. Consequently, elimination of these Cu-oxo clusters during reduction allows further distortion of the node.

Conclusion

In summary, by combining local and average structure probes we observed the dynamic structure of Cu-species supported on NU-1000 under conditions relevant to catalyst activation and catalysis. Despite the mobility of the reduced Cu-species, once formed, the Cu^0 particle dimensions do not grow further, suggesting that the NU-1000 framework effectively confines the Cu^0 nanoparticle dimensions. Here, the differently sized triangular and hexagonal channels of NU-1000 give rise to Cu^0 particles of two different sizes: sub-nanometer clusters and 4 nm nanoparticles.

Acknowledgements

This work was supported as part of the Inorganometallic Catalysis Design Center, an Energy Frontier Research Center

funded by the U.S. Department of Energy, Office of Science, Basic Energy Sciences under Award No. DE-SC0012702. Work done at Argonne was performed using the Advanced Photon Source, a U.S. Department of Energy (DOE) Office of Science User Facility operated for the DOE Office of Science by Argonne National Laboratory under Contract No. DE-AC02-06CH11357. A.E.P.P. acknowledges a *Beatriu de Pinós* fellowship (BP-DGR 2014) from the Ministry of Economy and Knowledge from the Catalan Government.

Notes and references

§ J.T.H. and O.K.F. have a financial interest in the start-up company NuMat Technologies, which is seeking to commercialize metal–organic frameworks.

1 1. A. Corma, *J. Catal.*, 2003, **216**, 298-312.
2 2. J. Lee, O. K. Farha, J. Roberts, K. A. Scheidt, S. T. Nguyen and J. T. Hupp, *Chemical Society Reviews*, 2009, **38**, 1450-1459.
3 3. J. Gascon, A. Corma, F. Kapteijn and F. X. Llabrés i Xamena, *ACS Catalysis*, 2014, **4**, 361-378.
4 4. S. M. Cohen, *J. Am. Chem. Soc.*, 2017, **139**, 2855-2863.
5 5. J. E. Mondloch, M. J. Katz, W. C. Isley Iii, P. Ghosh, P. Liao, W. Bury, G. W. Wagner, M. G. Hall, J. B. DeCoste, G. W. Peterson, R. Q. Snurr, C. J. Cramer, J. T. Hupp and O. K. Farha, *Nat. Mater.*, 2015, **14**, 512-516.
6 6. M. Rimoldi, A. J. Howarth, M. R. DeStefano, L. Lin, S. Goswami, P. Li, J. T. Hupp and O. K. Farha, *ACS Catalysis*, 2017, **7**, 997-1014.
7 7. D. Yang, S. O. Odoh, T. C. Wang, O. K. Farha, J. T. Hupp, C. J. Cramer, L. Gagliardi and B. C. Gates, *J. Am. Chem. Soc.*, 2015, **137**, 7391-7396.
8 8. Z. Li, A. W. Peters, V. Bernales, M. A. Ortuño, N. M. Schweitzer, M. R. DeStefano, L. C. Gallington, A. E. Platero-Prats, K. W. Chapman, C. J. Cramer, L. Gagliardi, J. T. Hupp and O. K. Farha, *ACS Central Science*, 2017, **3**, 31-38.
9 9. J. E. Mondloch, W. Bury, D. Fairen-Jimenez, S. Kwon, E. J. DeMarco, M. H. Weston, A. A. Sarjeant, S. T. Nguyen, P. C. Stair, R. Q. Snurr, O. K. Farha and J. T. Hupp, *J. Am. Chem. Soc.*, 2013, **135**, 10294-10297.
10 10. Z. Li, N. M. Schweitzer, A. B. League, V. Bernales, A. W. Peters, A. B. Getsoian, T. C. Wang, J. T. Miller, A. Vjunov, J. L. Fulton, J. A. Lercher, C. J. Cramer, L. Gagliardi, J. T. Hupp and O. K. Farha, *J. Am. Chem. Soc.*, 2016, **138**, 1977-1982.
11 11. D. Esken, S. Turner, O. I. Lebedev, G. Van Tendeloo and R. A. Fischer, *Chem. Mater.*, 2010, **22**, 6393-6401.
12 12. D. Esken, H. Noei, Y. M. Wang, C. Wiktor, S. Turner, G. Van Tendeloo and R. A. Fischer, *J. Mater. Chem.*, 2011, **21**, 5907-5915.
13 13. R. J. Comito, K. J. Fritzsching, B. J. Sundell, K. Schmidt-Rohr and M. Dincă, *Journal of the American Chemical Society*, 2016, **138**, 10232-10237.
14 14. C. K. Brozek, V. K. Michaelis, T.-C. Ong, L. Bellarosa, N. López, R. G. Griffin and M. Dincă, *ACS Central Science*, 2015, **1**, 252-260.
15 15. L. C. Gallington, I. S. Kim, W.-G. Liu, A. A. Yakovenko, A. E. Platero-Prats, Z. Li, T. C. Wang, J. T. Hupp, O. K. Farha, D. G. Truhlar, A. B. F. Martinson and K. W. Chapman, *J. Am. Chem. Soc.*, 2016, **138**, 13513-13516.
16 16. J. H. Cavka, S. Jakobsen, U. Olsbye, N. Guillou, C. Lamberti, S. Bordiga and K. P. Lillerud, *J. Am. Chem. Soc.*, 2008, **130**, 13850-13851.
17 17. G. J. Halder, K. W. Chapman, S. M. Neville, B. Moubaraki, K. S. Murray, J. F. Letard and C. J. Kepert, *J. Am. Chem. Soc.*, 2008, **130**, 17552-17562.
18 18. N. Planas, J. E. Mondloch, S. Tussupbayev, J. Borycz, L. Gagliardi, J. T. Hupp, O. K. Farha and C. J. Cramer, *J. Phys. Chem. Lett.*, 2014, **5**, 3716-3723.
19 19. I. S. Kim, J. Borycz, A. E. Platero-Prats, S. Tussupbayev, T. C. Wang, O. K. Farha, J. T. Hupp, L. Gagliardi, K. W. Chapman, C. J. Cramer and A. B. F. Martinson, *Chem. Mater.*, 2015, **27**, 4772-4778.
20 20. T. V. Ikuno, A.; Sanchez-Sanchez, M.; Ortuño, M. A.; Pahls, D. R.; Fulton, J. L.; Camaioni, D. M.; Li, Z.; Zheng, J.; Farha, O. K.; Hupp, J. T.; Cramer, C. J.; Gagliardi, L.; Lercher, J. A., *to be submitted.*, 2017.
21 21. A. P. Hammersley, S. O. Svensson, M. Hanfland, A. N. Fitch and D. Hausermann, *High Pressure Res.*, 1996, **14**, 235-248.
22 22. P. J. Chupas, K. W. Chapman, C. Kurtz, J. C. Hanson, P. L. Lee and C. P. Grey, *Journal of Applied Crystallography*, 2008, **41**, 822-824.
23 23. P. J. Chupas, K. W. Chapman, C. Kurtz, J. C. Hanson, P. L. Lee and C. P. Grey, *J. Appl. Crystallogr.*, 2008, **41**, 822-824.
24 24. A. Le Bail, *J. Non-Crsyt. Solids*, 1995, **183**, 39-42.
25 25. V. Petříček, M. Dušek and L. Palatinus, *Z. Kristallogr. Cryst. Mater.*, 2014, **229**, 345.
26 26. V. D. Petricek, M.; Palatinus, L., *Z. Kristallogr.* , 2014, **229**, 345-352.
27 27. A. A. Yakovenko, J. H. Reibenspies, N. Bhuvanesh and H.-C. Zhou, *J. Appl. Crystallogr.*, 2013, **46**, 346-353.
28 28. L. B. McCusker and C. Baerlocher, *Chem. Commun.*, 2009, 1439-1451.
29 29. A. A. Yakovenko, Z. Wei, M. Wriedt, J.-R. Li, G. J. Halder and H.-C. Zhou, *Crystal Growth & Design*, 2014, **14**, 5397-5407.
30 30. X. Qiu, J. W. Thompson and S. J. L. Billinge, *J. Appl. Cryst.*, 2004, **37**, 678.
31 31. C. L. Farrow, P. Juhas, J. W. Liu, D. Bryndin, E. S. Bozin, J. Bloch, T. Proffen and S. J. L. Billinge, *J Phys-Condens Mat*, 2007, **19**, 7.

32 32. A. E. Platero-Prats, A. Mavrandonakis, L. C. Gallington, Y. Liu, J. T. Hupp, O. K. Farha, C. J. Cramer and K. W. Chapman, *J. Am. Chem. Soc.*, 2016.

33 33. H. Imamura, M. Yoshinobu, T. Mihara, Y. Sakata and S. Tsuchiya, *Journal of Molecular Catalysis*, 1991, **69**, 271-280.

34 34. M. B. Gawande, A. Goswami, F.-X. Felpin, T. Asefa, X. Huang, R. Silva, X. Zou, R. Zboril and R. S. Varma, *Chem. Rev.*, 2016, **116**, 3722-3811.

35 35. R.-x. Zhou, T.-m. Yu, X.-y. Jiang, F. Chen and X.-m. Zheng, *Applied Surface Science*, 1999, **148**, 263-270.

36 36. S. Basahel, M. Mokhtar, E. Alsharaeh, T. Ali, H. Mahmoud and K. Narasimharao, *Catalysts*, 2016, **6**, 57.

37 37. J. Y. Kim, J. A. Rodriguez, J. C. Hanson, A. I. Frenkel and P. L. Lee, *Journal of the American Chemical Society*, 2003, **125**, 10684-10692.

38 38. A. Halder, S. Vajda, M. J. Pellin and S. Li, *unpublished results*.

39 39. A. Bilić, J. R. Reimers, N. S. Hush, R. C. Hoft and M. J. Ford, *J. Chem. Theory Comput.*, 2006, **2**, 1093-1105.

40 40. F. Wu, L. G. Qiu, F. Ke and X. Jiang, *Inorg. Chem. Commun.*, 2013, **32**, 5-8.

41 41. H. Y. Zhao, T. M. Nenoff, G. Jennings, P. J. Chupas and K. W. Chapman, *J. Phys. Chem. Lett.*, 2011, **2**, 2742-2746.

42 42. C. Rosler and R. A. Fischer, *CrystEngComm*, 2015, **17**, 199-217.

43 43. R. J. T. Houk, B. W. Jacobs, F. E. Gabaly, N. N. Chang, A. A. Talin, D. D. Graham, S. D. House, I. M. Robertson and M. D. Allendorf, *Nano Lett.*, 2009, **9**, 3413-3418.

44 44. H. Kobayashi, Y. Mitsuka and H. Kitagawa, *Inorg. Chem.*, 2016, **55**, 7301-7310.

45 45. C. Zlotea, R. Campesi, F. Cuevas, E. Leroy, P. Dibandjo, C. Volkringer, T. Loiseau, G. Férey and M. Latroche, *J. Am. Chem. Soc.*, 2010, **132**, 2991-2997.

46